RESEARCH ARTICLE

Key Points:
- Larsen C Ice Shelf is composed of distinct material units recording its dynamic and melt history
- Existing firn air model estimates commonly neglect the presence of buried low-density continental ice
- >40% of the firn zone of Larsen C is composed of refrozen ice in its central and northern sectors

Correspondence to:
D. W. Ashmore,
d.ashmore@liverpool.ac.uk

Ice and firn heterogeneity within Larsen C Ice Shelf from borehole optical televiewing

David W. Ashmore[1,2] , Bryn Hubbard[1] , Adrian Luckman[3] , Bernd Kulessa[3] , Suzanne Bevan[3] , Adam Booth[4] , Peter Kuipers Munneke[5] , Martin O'Leary[3], Heidi Sevestre[6] , and Paul R. Holland[7]

[1]Centre for Glaciology, Department of Geography and Earth Sciences, Aberystwyth University, Aberystwyth, UK, [2]School of Environmental Science, University of Liverpool, Liverpool, UK, [3]Geography Department, College of Science, Swansea University, Swansea, UK, [4]School of Earth and Environment, University of Leeds, Leeds, UK, [5]IMAU, Utrecht University, Utrecht, Netherlands, [6]School of Geography and Geosciences, University of St Andrews, St Andrews, UK, [7]British Antarctic Survey, Cambridge, UK

Abstract We use borehole optical televiewing (OPTV) to explore the internal structure of Larsen C Ice Shelf (LCIS). We report a suite of five ~90 m long OPTV logs, recording a light-emitting diode-illuminated, geometrically correct image of the borehole wall, from the northern and central sectors of LCIS collected during austral spring 2014 and 2015. We use a thresholding-based technique to estimate the refrozen ice content of the ice column and exploit a recently calibrated density-luminosity relationship to reveal its structure. All sites are dense and strongly influenced by surface melt, with frequent refrozen ice layers and mean densities, between the depths of 1.87 and 90 m, ranging from 862 to 894 kg m^{-3}. We define four distinct units that comprise LCIS and relate these to ice provenance, dynamic history, and past melt events. These units are in situ meteoric ice with infiltration ice (U1), meteoric ice which has undergone enhanced densification (U2), thick refrozen ice (U3), and advected continental ice (U4). We show that the OPTV-derived pattern of firn air content is consistent with previous estimates, but that a significant proportion of firn air is contained within U4, which we interpret to have been deposited inland of the grounding line. The structure of LCIS is strongly influenced by the E-W gradient in föhn-driven melting, with sites close to the Antarctic Peninsula being predominantly composed of refrozen ice. Melting is also substantial toward the ice shelf center with >40% of the overall imaged ice column being composed of refrozen ice.

1. Introduction

Ice shelves fringe much of Antarctica and are particularly sensitive indicators of environmental changes owing to their low elevation, low latitude, and exposure to both oceanic and atmospheric forcings. Ice shelves form when glaciers and ice streams flowing across the grounding line begin to float and spread laterally to fill an embayment. Once established by this core of continental ice, they are able to gain and lose mass at their upper and lower interfaces, as well as calving at the marine margin. Although, ice shelves are floating and therefore experience negligible basal shear stress, lateral stresses, and intermittent pinning to the seabed result in an ability to buttress grounded ice upstream. Through this, ice shelves modulate the contribution of the Antarctic Ice Sheet to eustatic sea level rise. Where ice shelves have thinned or collapsed, inflowing glaciers have accelerated and their discharge has increased accordingly [e.g., *Paolo et al.*, 2015; *De Rydt et al.*, 2015; *Scambos et al.*, 2004].

A critical characteristic of ice shelves is their predisposition to lose mass episodically once their geometry becomes unstable [*Kulessa et al.*, 2014]. The end-member of this behavior is a near-total disintegration of ice shelves, exemplified by the collapse of Larsen B Ice Shelf in early 2002 [*Scambos et al.*, 2003]. The disintegration of Antarctic Peninsula ice shelves has progressed poleward for the last ~30 years, commensurate with climate warming [*Cook and Vaughan*, 2010], and the mean annual isotherm of −9°C has been proposed as a practical limit of viability for ice shelves [*Morris and Vaughan*, 2003]. The largest remaining Antarctic Peninsula ice shelf, Larsen C Ice Shelf (LCIS), is intersected by this isotherm and may be currently experiencing surface melting conditions similar to those that preceded the collapse of its neighbors: Larsen A in 1995 and Larsen B in 2002. The surface of LCIS has lowered during the satellite era. Recent work has indicated that approximately half of this lowering signal is caused by the loss of air from the ice shelf firn [*Holland et al.*, 2015]. This air loss may be related to decreased surface accumulation or enhanced melting or firn compaction

associated with Antarctic Peninsula warming [*Turner et al.*, 2016]. Proposed mechanisms of ice shelf disintegration commonly invoke intense surface melting and ponding leading to flexure and (hydro)fracture [*Banwell et al.*, 2013; *Scambos et al.*, 2009]. In order for melt ponds to form, snowpack pore space must first be first filled [*Kuipers Munneke et al.*, 2014] or a substantial layer of impermeable refrozen (infiltration) ice must exist [e.g., *Machguth et al.*, 2016]. Distributed estimates of ice shelf thickness, a fundamental input into glaciological models, are typically derived through satellite altimetry by way of an assumption of hydrostatic equilibrium, requiring a correction to account for the proportion of the ice column not made up of pure ice. The term "firn air" is used to conceptualize both the mean density of the full ice column as the equivalent reduction in ice thickness if it were completely composed of bubble-free glacial ice and the pore space available for meltwater storage in the near surface. It is important to note that these definitions are not identical as material above the pore closure density and below the density of bubble-free glacial ice will contribute to firn air according to the former definition but not the latter.

Modeling commonly assumes pure bubble-free ice at depth [*Pritchard et al.*, 2012; *Chuter and Bamber*, 2015], and geophysical investigations [*Drews et al.*, 2016] typically prescribe a shape to the depth-density profile. However, recent results show that intense surface melt in one NW inlet on LCIS has led to an anomalously dense ~42 m thick layer of refrozen ice and an irregular density profile over the upper 97 m [*Hubbard et al.*, 2016]. Here the firn zone is ~10°C warmer and ~170 kg m^{-3} denser than would be expected without melt pond refreezing. The presence of this rheologically distinctive ice has implications for understanding and predicting ice shelf flow and fracture in warming regions. The stability of ice shelves also depends therefore on their large-scale three-dimensional structural composition and stress field. Surface mapping [*Glasser et al.*, 2009] and ground-penetrating radar surveys [*McGrath et al.*, 2014] show evidence of suture ice down-flow of coastal promontories and islands. This warmer, softer ice [*Dierckx and Tison*, 2013] is interpreted to form by the basal accretion of seawater in the lee of flow obstacles and appears farther down-flow to hinder the large-scale transverse propagation of brittle fractures such as basal crevasses [*McGrath et al.*, 2012] and rifts [*Jansen et al.*, 2015; *Kulessa et al.*, 2014].

The requirement for knowledge of the three-dimensional structure of ice shelves places a reliance on inferences from geophysical data or labor-intensive ice core drilling. Borehole hot-water drilling and optical televiewing (OPTV) is able to make a contribution to this requirement by being relatively rapid and logistically undemanding and, as a direct RGB image of the borehole wall is acquired, highly complementary to surface or airborne geophysical surveys. The aim of this paper is to investigate and report the internal structure of the sensitive north-central sector of LCIS. We present five borehole OPTV records, including and extending one presented and interpreted by *Hubbard et al.* [2016], thereby enabling spatially distributed ice characteristics to be considered in detail across the north-central sector of the ice shelf.

2. Field Site and Data

LCIS covers an area of ~50,000 km^2 [*Cook and Vaughan*, 2010] on the eastern Antarctic Peninsula (Figure 1). Föhn winds in the lee of the Graham Land mountains [*Elvidge et al.*, 2015] intermittently deliver warm air to the shelf, driving intense surface melt that occasionally forms melt ponds visible in synthetic aperture radar imagery [*Holland et al.*, 2011; *Luckman et al.*, 2014]. An analysis of data from weather stations located in the remnant Larsen B area indicates that the region has experienced föhn events of increased frequency and temperature over the last ~50 years, likely driven by a positive trend in the Southern Annular Mode [*Cape et al.*, 2015]. Airborne radar estimates of bulk firn air content indicate a near-complete depletion of firn air in the NW inlets, with firn air increasing eastward and southward [*Holland et al.*, 2011]. Repeated radar surveys along a transect through the center of LCIS show a loss of firn air averaging ~4 cm yr^{-1} during 1998–2012 [*Holland et al.*, 2015].

Study sites, illustrated in Figure 1, were selected in order to sample the evolution in ice properties along both N-S and E-W gradients. Three drill sites lie on a flow line emanating from Cabinet Inlet (CI) and two further drill sites lie on a flow line emanating from Whirlwind Inlet (WI). Boreholes are named according to their associated inlet and their approximate distance in kilometers along the flow line from the most inland borehole (Figure 1). CI-0, CI-22, and WI-0 are considered as "inlet sites" and CI-120 and WI-70 as "shelf sites." CI-0, presented by *Hubbard et al.* [2016], was drilled in November 2014 and the remaining four boreholes drilled in November and December 2015. All OPTV logs begin at 1.87 m depth, the length of the OPTV sonde, and reach depths of 90 or 97.5 m (Table 1).
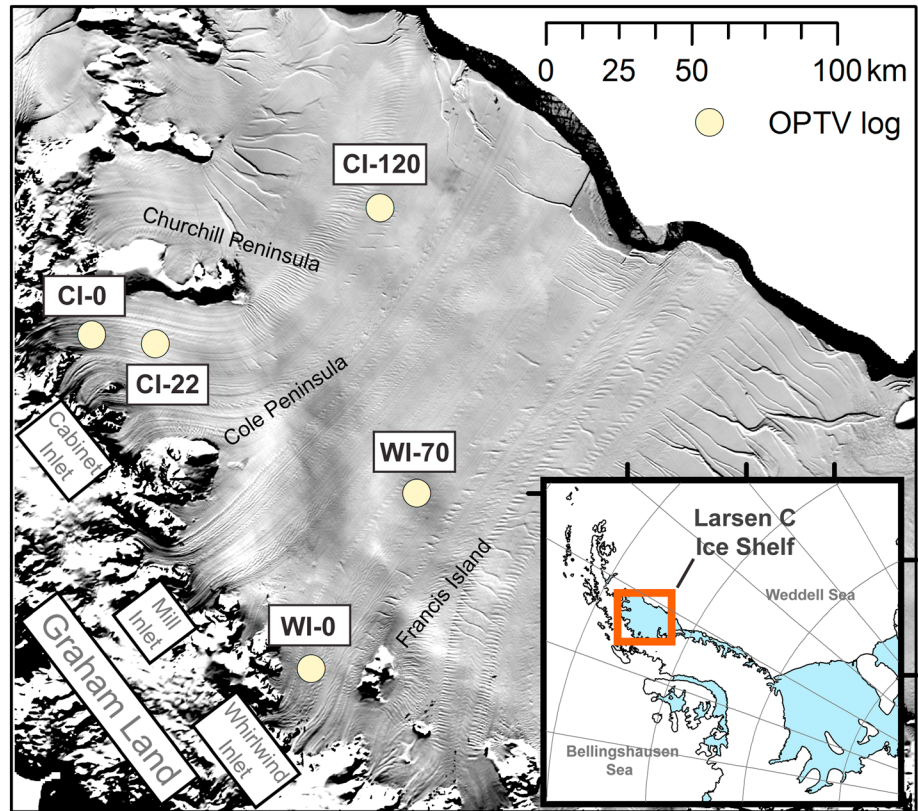
Figure 1. Location map of LCIS showing the sites of the OPTV borehole logs reported herein overlain on 2009 MODIS "MOA" image.

3. Methods

3.1. Hot-Water Drilling and Optical Televiewing

Pressurized hot water was used to drill boreholes of ~12 cm diameter. The ice column stratigraphy was logged by OPTV, previously described in detail by *Hubbard et al.* [2008]. The borehole wall is illuminated by a ring of 72 sonde-mounted light-emitting diodes (LEDs), while a downward looking CCD camera records a reflected image on a hyperboloidal mirror. This results in a geometrically accurate RGB image of the complete borehole wall which can be visualized as a 3-D "virtual core." As the borehole is solely illuminated by stable sonde-mounted LEDs, image brightness is a measure of borehole wall reflectivity. Elsewhere in Antarctica, OPTV has been used successfully in boreholes to identify facies associated with a rift on Roi Baudouin Ice Shelf (RBIS), including the identification of marine ice and infiltration ice layers [*Hubbard et al.*, 2012]. The OPTV image resolution is defined during acquisition with higher resolution necessitating a reduced vertical logging rate. For our images we sample 360 pixels in each row and sample the borehole vertically every 1 mm. The exception to this is CI-22 where a 2 mm vertical sampling rate was used due to inclement weather conditions during acquisition.

3.2. Density Derivation and Error

Borehole image brightness averaged by pixel row, or "OPTV luminosity," provides a proxy for firn and ice density on decameter scales [*Hubbard et al.*, 2013]. The underlying principle, presented in detail by *Hubbard et al.* [2013], is that borehole reflectance decreases with density under a stable

Table 1. Site Locations and Depths

Site	Start (m)	Depth (m)	Location
CI-0	1.87	97.5	−66.403, −63.376
CI-22	1.87	90	−66.588, −63.212
CI-120	1.87	90	−67.000, −61.486
WI-0	1.87	90	−67.444, −64.953
WI-70	1.87	90	−67.500, −63.336

light source. Transmitted sunlight is not considered to influence the OPTV logs reported herein because all logs begin ~1.87 m deep in snow and firn, by which point sunlight has been attenuated to negligible values [e.g., *O'Neill and Gray*, 1973]. The general luminosity-density relationship determined by *Hubbard et al.* [2013] was

$$\rho = 910 - 17.2e^{(0.012L)}\left(R^2 = 0.96\right), \tag{1}$$

where L is OPTV luminosity [*Malone et al.*, 2013]. However, the OPTV probe used for the calibration presented in equation (1) has since been replaced by an improved model. The replacement OPTV probe was newly calibrated, reported by *Hubbard et al.* [2016], on the basis of densities measured on samples recovered from a more recent borehole cored on the RBIS [*Philippe et al.*, 2016]. This new calibration, applied to the OPTV logs reported herein, is

$$\rho = 950 - 40.1e^{(0.0101L)}\left(R^2 = 0.82\right). \tag{2}$$

While equation (2) was determined on the basis of a borehole cored on RBIS, the densities derived from it are based on OPTV logs from boreholes drilled on LCIS. Such a transfer may introduce calibration errors arising from different material properties between the two sites, such as snow and ice crystallography and impurity composition and concentration. In order to estimate this error, we revisit the initial OPTV luminosity-density calibration reported by *Hubbard et al.* [2013], which combined independent calibrations from two separate boreholes from contrasting locations: one on Derwael Ice Rise and one on RBIS. In order to approximate calibration transfer error we apply the calibration from each of those two boreholes to the OPTV luminosities of the other and compare the resulting OPTV-derived densities with the (actual) gravimetrically measured densities. This yields root-mean-square differences of 58.2 kg m^{-3} over the density range of 481–700 kg m^{-3} ($n = 18$), 26.0 kg m^{-3} over the density range of 700–800 kg m^{-3} ($n = 10$), and 15.0 kg m^{-3} over the density range of 800–904 kg m^{-3} ($n = 26$). These values account for both the calibration error and the error in transferring the calibration from one borehole to another. Errors may also be methodologically exaggerated by unavoidable slight differences in the core and OPTV depth scales used in the calibration, as discussed by *Hubbard et al.* [2013].

An additional source of error in the OPTV-derived densities reported herein derives from calibration boreholes being cored mechanically, while our LCIS boreholes were drilled by hot water. It is therefore likely that drilling water may have altered the imaged snow and firn by freezing onto, or seeping into, the borehole wall. This potential error remains unconstrained but is considered to be minor for several reasons. First, there is no change in OPTV luminosity coincident with the water level within our boreholes. Second, near-surface borehole inspection indicates that hot water drilling does not darken the snow and firn forming the borehole wall. Third, OPTV logging successfully imaged ice layers and lenses, including within low-density, near-surface snow and firn. Finally, although unconstrained, any drill water present within, or ice formed on, the borehole wall would likely darken the image and therefore act to increase apparent density.

Slight coaxial misalignment of the OPTV sonde and irregularities in the borehole shape, most notably by drill hose incision into soft snow and firn of the upper sections of CI-22 and WI-70, result in occasional anomalously dark regions of some OPTV sections. This effect is caused by the narrow, incised notch being more-weakly illuminated and appearing as a quasi-vertical "shadow" on the complete OPTV log. To minimize this effect on our estimated density profiles we reject the upper and lower quartile brightness values on each row when calculating luminosity. In order to test the effect this step has on our derived densities we subtract the edited from the unedited density profile. This demonstrates that the removal of these extreme regions results in a very minor increase in the derived density. Across all logs the mean difference is -0.01 ± 3.30 kg m^{-3}. In the upper part (1–30 m) of WI-70, where hose incision is most apparent, the mean difference is -1.15 ± 2.50 kg m^{-3}.

Firn air volume fraction (ϕ) is estimated for each depth bin from the OPTV-derived density (ρ) where the density of glacial ice is taken as $\rho_i = 917$ kg m^{-3} by

$$\phi = 1 - \frac{\rho}{\rho_i}. \tag{3}$$

To estimate firn air content of the upper 1.87 m, which is not recorded by OPTV due to the length of the sonde, we use 0.6 m deep snow pits at CI-0, CI-60 (i.e., 60 km along flow line), and CI-120. Here density

was measured gravimetrically using a cylindrical cutter [see *Procksch et al.*, 2016] at 0.05 m increments yielding a mean density of 357 ± 8.8 kg m^{-3}. We then assume a linear increase in density from this value to the mean OPTV-derived density in the upper 0.1 m of the OPTV log and add this to our OPTV-derived firn air thickness. Throughout we use the term "firn air" to refer to the pore space throughout the ice column regardless of whether the material is snow, firn, or ice and assume that the mass of air within the pore space is negligible.

3.3. Ice Character and Classification

Ice character is a function of (i) surface conditions at and shortly after deposition and (ii) post burial compaction-metamorphism and deformation. The principle adopted here is that spatiotemporal differences in these processes lead to classifiable ice units. Our approach is to describe ice character based on layer style (i.e., thickness, brightness, dip, and edge characteristics), density characteristics, and depth without assigning a genetic mechanism. These can then be interpreted subsequently in terms of physical processes and environments. While some environments lead to distinct material facies contrasts [e.g., *Hubbard et al.*, 2012] others lie upon a spectrum where the effect of a particular process becomes increasingly dominant.

3.4. Image Thresholding and Infiltration Ice Estimation

Three principal processes affect the stratigraphy of ice shelves. The accumulation of snow may result in quasi-regular surface-parallel layering reflecting depositional differences during accumulation, often referred to as primary stratification in structural glaciology [*Hudleston*, 2015]. Second, the snowpack undergoes depth-related densification by compaction-metamorphism driven by snow temperature and the weight of the overlying snow. Third, surface meltwater that percolates into a cold snowpack refreezes to form bubble-poor, dense infiltration ice, identifiable as dark (low reflectance) layers in OPTV logs. Furthermore, ice inherited from inland may also be overprinted during a variety of brittle and ductile deformation processes relating to dynamic flow, for example, by the incorporation of debris [*Glasser et al.*, 2014] or platelet ice of marine origin [*Hubbard et al.*, 2012].

Primary stratification in our LCIS OPTV logs is typically faint and disrupted by melt processes (see section 4.1), so we can consider OPTV images to comprise chiefly of infiltration ice layers overprinted onto a densifying host material. The resulting bimodal distribution of pixel brightness lends itself well to image thresholding analysis [e.g., *Kinnard et al.*, 2008] which allows the consistent and reproducible identification of infiltration ice layers. However, it is important to consider the ice unit when interpreting thresholding results. Where ice is relatively homogenous, other features that may arise from trapped bubbles, incorporated debris, or healed fractures may be identified by the algorithm. In this case the threshold-identified layers do not coincide with refrozen ice layers.

Uneven illumination is a well-known issue in the successful application of thresholding algorithms. Here we prepare our OPTV logs prior to thresholding in order to minimize lateral and vertical biases in image brightness not related to glaciological features and maximize the effectiveness of image thresholding. Areas of anomalous illumination were removed by row (section 3.2), and images were smoothed with a 1×10 pixel-wide median filter to highlight vertical gradients in brightness. Images were detrended with a sum-of-sine function fitted to the luminosity profile in order to remove long-wavelength density variations with depth (Figure 2). Thresholding was then performed sequentially on 2 m long image sections to achieve optimal results as some minor long-wavelength variations in image brightness remain with depth even after detrending. Three common autothresholding algorithms were tested by trial and error: those of *Ridler and Calvard* [1978], *Kittler and Illingsworth* [1986], and *Otsu* [1979]. *Otsu*'s [1979] method performed most consistently and was adopted for this investigation.

Otsu's [1979] autothresholding technique divides a given distribution's population into two clusters based on a threshold value and calculates the difference between these clusters. The optimal threshold is arrived at by finding the values at which the maximum difference between these clusters is attained. The result is a binary image in which each pixel is classified as either low or high brightness. For our application, any pixel row classified as over 90% low brightness is identified as "dark" (Figure 2), allowing OPTV image segments to be characterized in terms of a darkness index, given by the percentage of their length classified as dark.
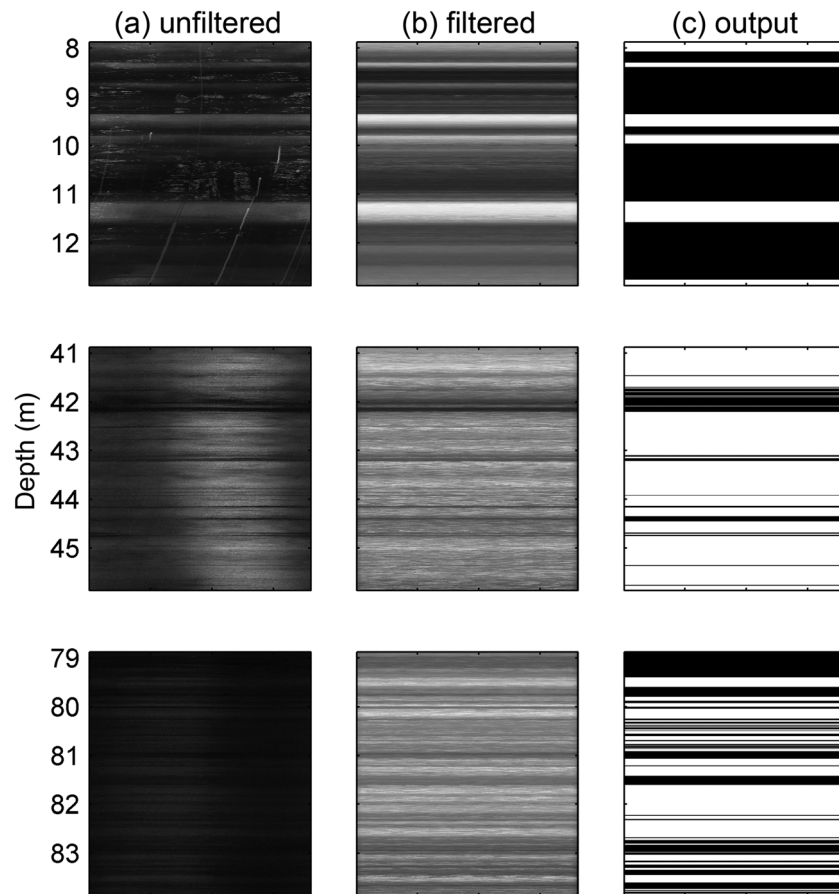
Figure 2. Stages of thresholding as applied to three environments (figure rows) from the CI-120 OPTV borehole log. Columns show (a) raw OPTV log; (b) the result of the rejection of upper and lower quartile values by row, vertical detrending and the application of the median filter; and (c) the result of thresholding to reveal the dark layer population.

4. Results

4.1. OPTV Borehole Logs and Density Profiles

Optical televiewer logs and the derived density profiles from the northerly Cabinet Inlet flow line are presented in Figure 3 and those from the more southerly Whirlwind Inlet in Figure 4. Borehole logging reveals the presence of layers and distinct units across all five sites with several logs displaying clear, visually identifiable step changes in style (explored further in section 4.2). The ice column of LCIS varies in both N-S and E-W directions in terms of layer presence, layer style, contrast between layers and host ice, and the decrease in host ice brightness with depth. Bright host ice is increasingly present in the easterly (seaward) and southerly directions, particularly in the upper part of the logs, while dark, homogenous ice is increasingly present in the westerly (inland) and northerly directions. All the LCIS logs contrast strongly with OPTV logs from other polar ice masses, including Derwael Ice Rise and Roi Baudouin Ice Shelf, East Antarctica [*Hubbard et al.*, 2013], and Summit, Greenland [*Hubbard and Malone*, 2013]. In these logs images darken gradually with depth, discrete dark layers are infrequent and faint regular banding is commonly visible. Such an "uninterrupted" pattern is entirely absent from any of our LCIS borehole logs.

The mean density from all our sites is 873.1 ± 39.2 kg m^{-3}, which is denser and less variable than RBIS where mean OPTV-derived density at depths of between 1.87 and 66.1 m is 742.4 ± 86.8 kg m^{-3} [*Hubbard et al.*, 2013]. The spatial variation in firn/ice column identified visually is reflected in the luminosity-derived density results (summarized in Table 2). These demonstrate that CI-22 has the highest mean density and WI-70 the lowest mean density, although only separated by 32.6 kg m^{-3}. Density standard deviation indicates that CI-22 has the least variable ice and firn column, while WI-70 has the most variable profile. Firn air content affirms this
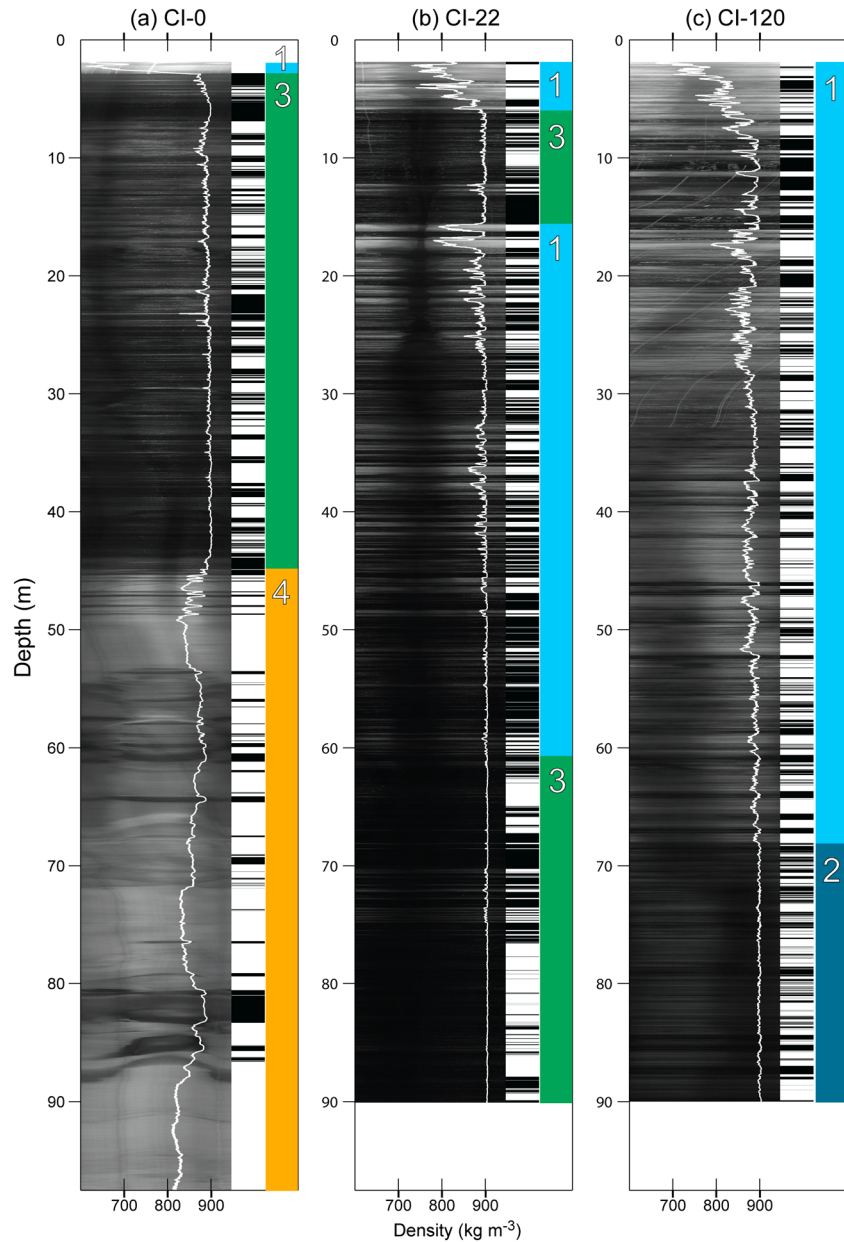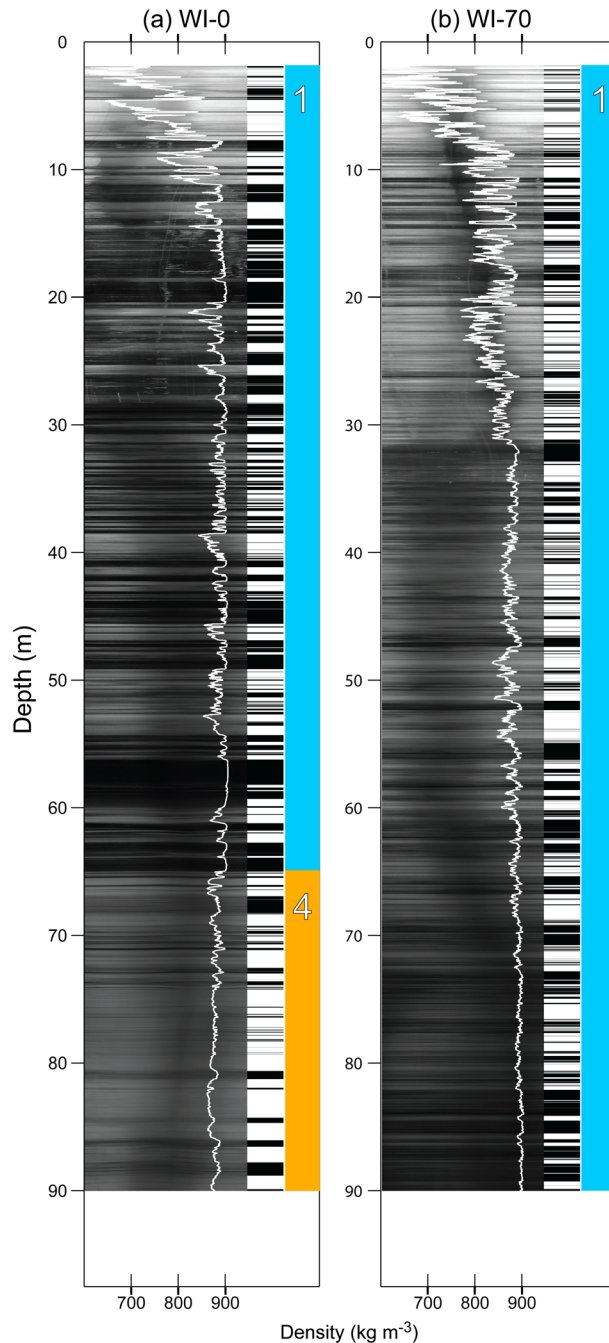
Figure 3. (left) Borehole OPTV raw logs and density profiles, (middle) binary thresholding output, and (right) unit classification from sites (a) CI-0, (b) CI-22, and (c) CI-120 (locations given in Figure 1).

spatial pattern as it is directly calculated from density. With the exception of CI-0, a spatial pattern in the large-scale near-surface density of LCIS emerges with the densest ice located toward the north and inland portions of the ice shelf, becoming progressively less dense southward and toward the calving margin. CI-0 and WI-0 both host a density inversion at ~45 m and ~65 m depth, respectively (Table 3). Using a 2 m moving average of density, we estimate the depth to the pore closure density of 830 kg m^{-3} (Table 2). This is important because it represents the maximum depth to which percolating meltwater can reach before refreezing. Despite the lower mean density of CI-0, the pore closure depth from this site conforms to the W-E and N-S pattern, due to the thick layer of impermeable refrozen ice at 2.9 m depth, as noted by *Hubbard et al.* [2016].

4.2. Classification of Ice Type

Four units are defined on the basis of characteristics revealed by the OPTV logs (Figures 3–7), named U1–U4 with increasing number broadly referring to increasing depth within the ice column, although not all ice

Figure 4. (left) Borehole OPTV raw logs and density profiles, (middle) binary thresholding output, and (right) unit classification results from (a) WI-0 and (b) WI-70 (locations given on Figure 1).

types are present at all sites. U1 is always present at the ice surface, and U4, where present, is always located at the log base. The distribution of units with depth is presented in Figure 3 (Cabinet Inlet flow line) and Figure 4 (Whirlwind Inlet flow line) and summarized in Table 3.

U1 is present in all logs as the uppermost unit and is characterized by depth-darkening host material over meter scales, containing frequent dark layers which may be centimeters to decimeters thick (Figures 5a–5f). The brightness of dark layers also decreases with depth; e.g., Figure 5a shows clearly identifiable dark layers, but they are not as prominent as those in Figure 5c or 5e. Host material darkening rates within U1 are also site specific, such that U1 at CI-120 is darker than U1 at WI-70 at similar depths (cf. Figures 5b and 5c and Figure 3).

U2 occurs exclusively at the base of CI-120 and is distinct from the overlying ice by a decrease in contrast between host material and layers due to darkening of the normally bright host material. Structure remains visible in U2 sections, especially after image enhancement (Figure 6), as relatively dark layers overprinted on a lighter host material similar to those present within U1.

U3, similar to U2, is generally dark but contrasts with both U1 and U2 in that it is not characterized by persistent, well-defined layering (Figures 7a–7k). U3 is present only at CI-0, where it forms a near-surface unit 41.57 m thick, and at CI-22 where two sections of U3 are present, one 9.74 m thick and the other >28.32 m thick located lower in the log (Figure 3). Structure is visible in U3 OPTV logs as bright speckles that form clouds, layers, and, in one case, vertical streaks not found in any other unit (Figures 7a and 7g). Any layering present within U3 is commonly diffuse and faint (e.g., Figures 7c and 7h) but can occasionally be well defined (Figures 7d and 7i). No evidence of internal structure is seen in the raw OPTV log of the basal section of U3 at CI-22 (Figures 7e and 7f). Upon image enhancement, however, some speckling and occasional layers can be seen relative to the background host material, similar in form to those observed in U3 higher in the ice column (Figures 7j and 7k). The boundary between U3 and overlying units is abrupt where U3 is shallow (CI-0 at a depth of 2.90 m and CI-22 at a depth of 5.90 m), while the deeper transition (CI-22 at a depth of 68.56 m) is less distinct due to darker U1 material above it. Here the transition is marked by a paucity of regular light/dark layering and a reappearance of

Table 2. Summary of Density Characteristics From LCIS Boreholes[a]

Site	Log Mean Density (±1σ) (kg m^{-3})	Firn Air Content (m)	Firn Air Content (Surface Corrected, m)	Pore Closure Depth (m)
CI-0	872.2 ± 30.4 (868.3 ± 32.0)	4.31 (5.08)	5.18 (5.95)	3.29
CI-22	894.2 ± 21.8	2.20	2.87	4.18
CI-120	879.0 ± 27.7	3.65	4.46	6.05
WI-0	873.2 ± 42.7	4.21	4.99	7.67
WI-70	861.6 ± 51.8	5.32	6.18	8.43

[a]Mean density and firn air content are calculated over the common depth range of 1.87–90.00 m for all logs and 1.87–97.50 m for CI-0 (parenthesized). Surface-corrected firn air content refers to the firn air content plus the air contained within the upper 1.87 m. Pore close off density is taken as 830 kg m^{-3}.

speckled ice (Figure 7k). We note a reappearance of layering ~70 to ~75 m within U3 at CI-22 which may reflect a return to conditions somewhat similar to those forming U1 at shallower depths. Given that this sequence of layers is between two thick sections of dark speckled ice, which is also present between the layers themselves (Figures 7e and 7j) we opt to classify this whole section as U3. The base of U3, where imaged at CI-0, is moderately abrupt and followed by a reappearance of dark layers against a lighter host material.

U4 is characterized by an increase in brightness with depth, yielding an equivalent decrease in luminosity-derived density in this unit (Table 3). U4 is only present at CI-0 and WI-0, located closest to the mouths of the two inlets (Figure 1). U4 contains steeply dipping layers (Figure 8), sporadic decimeter-thick dark layers (Figures 8a and 8b) and meter-thick sections of undisrupted ice (e.g., Figures 8f and 8l). Layers of different styles cut across one another, as shown in Figures 8a, 8d, 8e, and 8f. These dipping layers may have diffuse edges (Figures 8b and 8e) or be well defined (Figure 8d). These U4 layers and features are also not exclusively planar; e.g., Figures 8b and 8h show a dipping bright layer beginning at ~57.5 m depth at CI-0 associated with a lighter region at a depth of between 57.2 and 57.5 m. In WI-0 (Figures 8c and 8h) a brighter layer at ~63.9 m appears to branch, resulting in a spur centered at 63.4 m. In both CI-0 and WI-0 U4 extends beyond the base of the log, and the unit's total thickness is unknown (Table 3).

4.3. Image Thresholding

Image thresholding results are summarized in Table 3 and displayed in Figure 3 for Cabinet Inlet and Figure 4 for Whirlwind Inlet. In those sections where the brighter host material is overlain by darker, low reflectance layers, our thresholding algorithm performs well, with identified layers corresponding closely to those identifiable by eye (Figure 2). However, in cases of reduced density contrast between melt layers and host ice the algorithm is not as successful at identifying visually identified melt layers. Where ice is composed of a less dense host ice overprinted by dense refrozen ice layers, the proportion of ice column composed of refrozen material is given by its darkness index value (Table 3).

Table 3. Summary of Units, Unit Density, and Darkness Percentage Results From LCIS Borehole OPTV Logs

Site	Unit	Depth Range (m)	Darkness Index (%)	Mean Density (±1σ) (kg m^{-3})	Firn Air (m)	Unit Thickness (m)
CI-0	U1	1.87–2.90	6.5	696.3 ± 67.0	0.25 (1.12)	1.03 (2.90)
	U3	2.90–44.87	47.7[a]	892.5 ± 7.1	1.12	41.97
	U4	44.87–97.50	17.3	852.4 ± 21.0	3.71	52.63[b]
CI-22	U1	1.87–5.90	29.9	822.9 ± 37.4	0.41 (1.08)	4.03 (5.90)
	U3	5.90–15.64	66.0[a]	896.7 ± 5.4	0.22	9.74
	U1	15.64–61.68	62.8	893.5 ± 16.4	1.18	46.04
	U3	61.68–90.00	39.6[a]	904.4 ± 1.5	0.39	28.32[b]
CI-120	U1	1.87–68.56	41.5	872.6 ± 29.0	3.23 (4.04)	66.69 (68.56)
	U2	68.56–90.00	41.0	899.0 ± 2.1	0.42	21.44[b]
WI-0	U1	1.87–64.95	53.2	871.7 ± 50.1	3.11 (3.89)	63.08 (64.95)
	U4	64.95–90.00	27.5	876.8 ± 7.6	1.10	25.05[b]
WI-70	U1	1.87–90.00	44.1	861.6 ± 51.2	5.32 (6.18)	88.13 (90.00)[b]

[a]U3 where assumption of bright background and dark layering is not valid.
[b]The base of the unit is unknown. Parenthesized thicknesses and firn air contents represent values with the uppermost 1.87 m (not sampled by OPTV log) included.
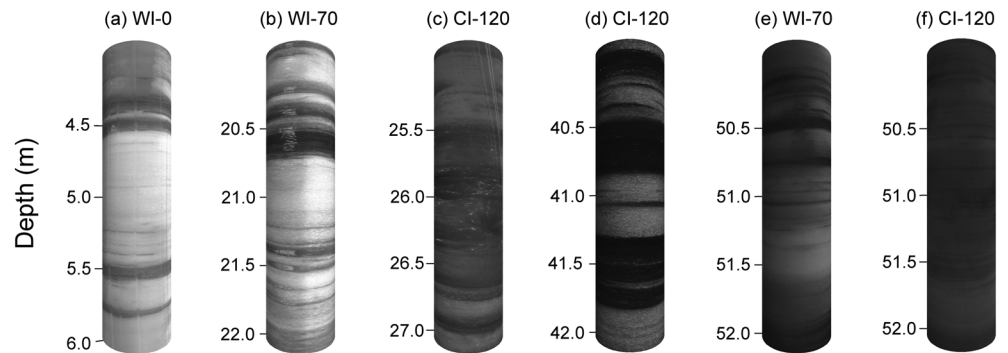
Figure 5. (a–f) Rolled virtual core images of U1 in LCIS borehole OPTV logs, arranged by depth. Borehole locations are given at the top of each panel.

U1 has a darkness index ranging from 6.5% at CI-0 to 53.2% WI-0. U2 has a darkness index at CI-120 of 41.0%. In both U1 and U2 observed layers correspond closely with threshold-identified layers. In U3 the typical host/layer configuration is not present and the thresholding algorithm identifies the absence of speckle clouds and layers rather than the presence of dark layers, resulting in a darkness percentage of 47.7% at CI-0. At CI-22 the upper occurrence of U3 has a darkness percentage of 66.0% and the lower occurrence has a darkness percentage of 39.6%. U4 has darkness percentages of 17.3% at CI-0 and 27.5% at WI-0.

5. Interpretation and Discussion

### 5.1. Interpretation of Material Units

The framework for the interpretation of OPTV logs in terms of physical conditions and processes is guided by research indicating that LCIS is strongly influenced by föhn winds [*Elvidge et al.*, 2015], which drive intense surface melting and ponding [*Holland et al.*, 2011; *Luckman et al.*, 2014]. Föhn-driven melting is focused on the inland zone of the ice shelf, although some melt occurs across almost all of LCIS during summer [*Luckman et al.*, 2014; *van Wessem et al.*, 2016]. Therefore, our interpretative framework is designed to accommodate the OPTV signature of (i) inland-focused, intense, episodic föhn-driven melt and (ii) spatially widespread seasonal melting of variable intensity.

U1 represents snow and firn accumulated on the ice shelf that is progressively undergoing compaction-metamorphism and moderate melt infiltration and refreezing. These processes lead to a unit in which the host material is densifying and interrupted sporadically by layers of refrozen melt or infiltration ice. This observation confirms that substantial melting, meltwater percolation, and refreezing on LCIS have been occurring for many decades. The uppermost 1.87 m is not sampled by the OPTV log, but snow-pit and drilling records indicate that this zone is also composed of U1 ice. Thus, U1 has a thickness of 64.95 m at CI-120 and >90 m at WI-70. It is relatively thin at CI inland sites as föhn-driven melting and percolation events change the

ice character to U3 (discussed below) to prevent the accumulation of a thick U1 layer. In this context, we also note that CI-0 was logged by OPTV in November 2014, while all others were logged in November/December 2015 and that melt ponds were visible in Cabinet Inlet in March 2015. Thus, U1 is 2.90 m thick at CI-0, where it immediately overlies an impermeable U3 layer. At CI-22 U1 both overlies (to 5.90 m) and underlies (from 15.54 m) such a U3 layer. In contrast, at WI-0, where U1 is not underlain by near-surface U3, U1 extends to a depth of 64.95 m. Directly above the U1/U4 boundary at WI-0 there is a notable dark, dense layer at a depth of ~57.5 m to 60 m, probably related to a short period of intense melting close to the grounding line of
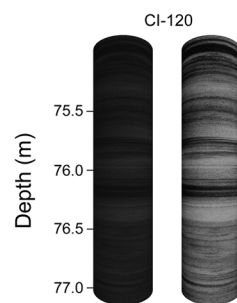
Figure 6. (left) Rolled virtual core image of U2 in CI-120 borehole OPTV log in its native brightness and with (right) enhanced contrast.
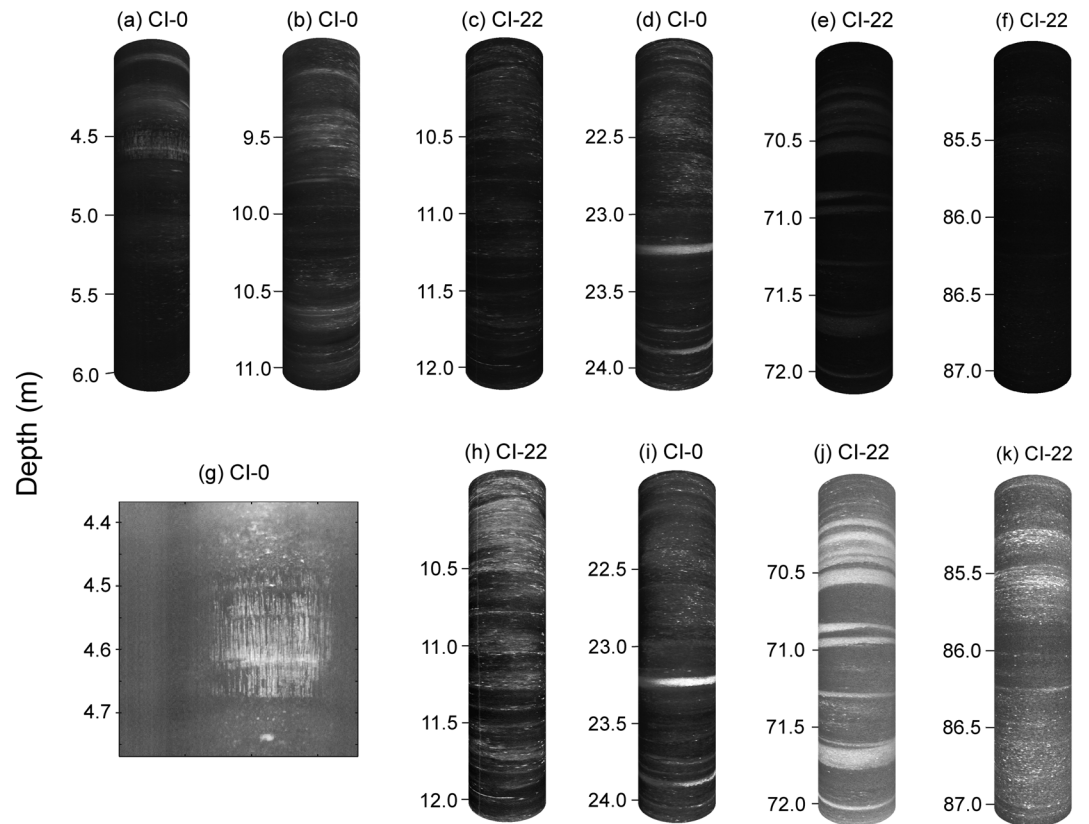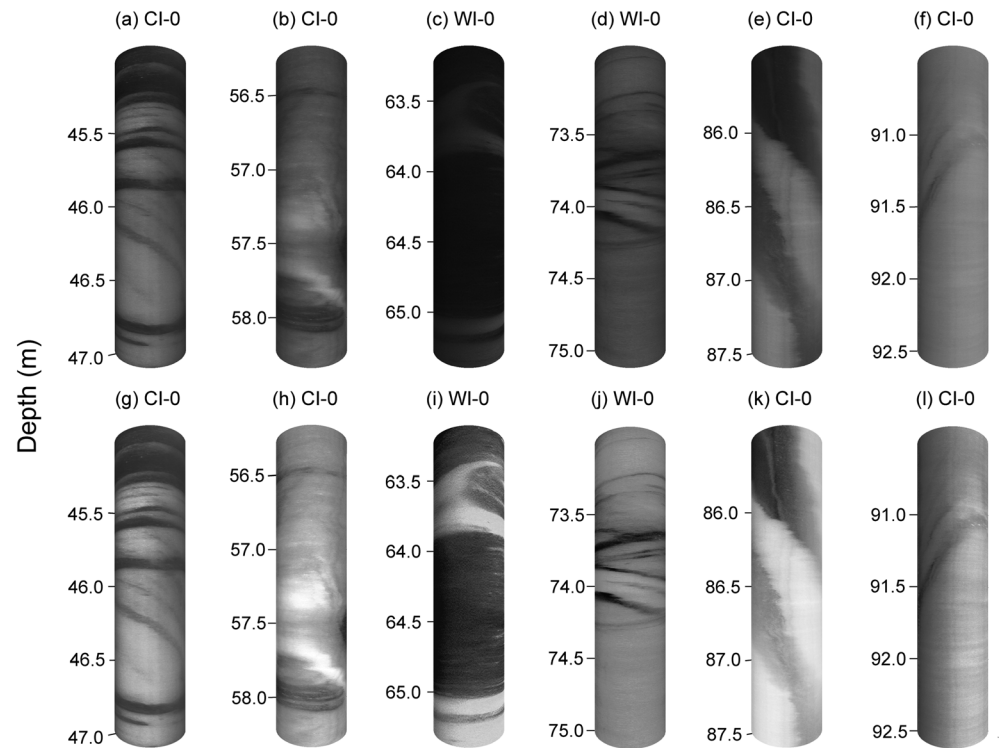
Figure 7. (a–f) Rolled virtual core images of U3 in LCIS borehole OPTV logs, arranged by depth, with (g–k) enhanced images. Note that Figure 7g is not rolled to better display features. Borehole locations are given at the top of each panel.

WI, but more limited than that forming U3 in CI. Melt layers are present throughout U1 at all sites, including shelf sites (i.e., CI-120 and WI-70; see section 2), which, beneath the upper few meters, must be many decades old, given the typical accumulation in this area of 0.3–0.7 m water equivalent per year [*van Wessem et al.*, 2016]. This indicates that U1 ice is formed by spatially widespread summer melting on an accumulating ice shelf, rather than being driven by föhn events restricted to inlet locations.

U2 is present exclusively at the base of CI-120, and its boundary with the overlying U1 is identified by a slight but notable step change in image brightness (Figure 3). U2 is material that has experienced enhanced firnification due to either föhn-driven melting, not sufficiently intense to form melt ponds (cf. discussion of U3 below), or due to climate variability not directly attributable to föhn events along the flow line. U2 formation at CI-120 is unlikely to be directly related to föhn melting as it would have been at the surface downstream of the region considered to be strongly affected by föhn events [*Luckman et al.*, 2014]. *van Wessem et al.* [2016] argued that topography exerts a strong control over the local meteorology of the eastern Antarctic Peninsula. Therefore, the transition to U2 ice may partially reflect the movement of ice away from the influence of topographic features (e.g., Churchill Peninsula, Cole Peninsula, and Francis Island; Figure 1) and toward open ice shelf conditions. Regardless of the precise mechanism, this warming drives increased densification of the host material. Despite the dense host ice, refrozen layers are visible throughout U2 (Figure 6) after image enhancement and appear to be successfully identified by our thresholding algorithm. There is a potential for equifinality as U1 will densify toward material with a U2-like appearance, and there is unlikely to be a clear spatial limit of föhn melting or on the effect of local topographic features. Nevertheless, in the absence of further information we provisionally distinguish U1 from U2 on the basis of the apparent step-change in host/layer density contrast at the contact between the two at CI-120.

Our analysis of the OPTV properties of U3 is consistent with its interpretation as "pond ice" [*Hubbard et al.*, 2016] formed proximal to the location of maximum föhn warming. Here meltwater is abundant enough to refreeze into a vertical series of near-continuous units of massive ice and the meltwater may pool to form

Figure 8. (a–f) Rolled virtual core images of U4 in LCIS borehole OPTV logs, arranged by depth, and replicated with (g–k) enhanced contrast. Borehole locations are given at the top of each panel.

surface melt ponds prior to refreezing. The exact mechanism of U3 formation must allow water in the snowpack to become sufficiently mobile to percolate to the previous U1/U3 interface. In this way, U3 is built up episodically after periods of extreme melt. Our interpretation of U3 being formed by a significant volume of mobile liquid water is supported by features visible in the OPTV logs. For example, at CI-0 at a depth of 4.6 m (Figures 7a and 7g) a quasi-vertical bright streaking feature is observed. This is interpreted as being formed by an upper and lower freezing-front rejecting dissolved gases and forming two coalescing vertical bubble trains, characteristic of the linear progression of a freezing front through standing water [*Hubbard*, 1991]. The bright speckles that are present throughout U3 are interpreted as bubble clouds. Typically, these bubbles form into layers and vary in prominence, as seen at a depth of 22–24 m at CI-0 (Figure 7d).

U4 is ice formed upstream of the zone of föhn-driven melting at an inland location of sufficient elevation to experience reduced surface melt intensity. Since U3 ice is interpreted to form though intense föhn-driven melting, the surface outcrop of the boundary between U3 and U4 likely corresponds broadly with the grounding line. This interpretation is supported by the presence of steeply dipping layers of up to several meters thick and of variable brightness, which we interpret as healed crevasses and other layers having experienced ductile deformation as ice passes over the grounding line. These features are more abundant at CI-0 (Figure 3) than at WI-0 (Figure 4), possibly due to the configuration of feeder glaciers in CI leading to a more compressive regime than in WI (Figure 1). U4 is potentially comparable to the "continental ice" reported by *Craven et al.* [2005] within Amery Ice Shelf. Similar to Amery, this unit, discounting its contorted layers, is bubble-rich and less dense relative to the overlying unit.

5.2. Spatial Variability of Firn Air Content and Refrozen Ice

The pattern of firn air distribution estimated from our OPTV logging (Table 2) is broadly consistent with the pattern identified by *Holland et al.* [2011]. These authors used radar travel time to decompose ice shelf thickness into its component parts of pure ice and air. Their results, and ours between the depths of 0 and 90 m parenthesized for reference, indicate an increase in firn air from 3.0 (5.18) m at CI-0, 6.5 (2.87) m at CI-22,

10.2 (4.21) m at WI-0, and 10.6 (3.65) m at CI-120 to 12.0 (5.32) m at WI-70. As we only estimate firn air in the upper ~90 m of the ice shelf we cannot compare our data exactly to those of *Holland et al.* [2011]. One notable exception to this spatial correspondence is CI-0, where U4 leads to an estimated firn air content larger than that reported by *Holland et al.* [2011] for the entire ice column. This is surprising because some firn air will certainly be contained in the ice column beneath the maximum OPTV sampling depth. Interpreting OPTV-derived density in terms of firn air relies on the luminosity-density relationship of *Hubbard et al.* [2016]. At high densities ($> ~700$ kg m^{-3}) the RMS error of this relationship is between 15 and 26 kg m^{-3} (section 3.2 above) which appears to be randomly distributed. Converting this to firn air in a worst case for CI-0, in which the mean density is incorrect by ± 26 kg m^{-3}, results in an uncertainty of ± 2.5 m of firn air to 90 m ice depth, while an error of ± 15 kg m^{-3} results in ± 1.4 m of firn air. When interpreted in conjunction with the reported error of ± 1.8 m by *Holland et al.* [2011] our results are within error of each other. A further consideration is that CI-0 is in an area of elongate melt pond formation, so strong lateral variations in density structure likely exist in the near surface. Despite the uncertainties relating to the absolute density the profile of relative brightness revealed by luminosity alone indicates that a substantial proportion of firn air is contained within continental ice at depth, at least at CI-0, as well as being trapped between refrozen layers at other sites.

In cases where altimetric data are used to reconstruct ice shelf thickness or thickness change [e.g., *Pritchard et al.*, 2012; *Chuter and Bamber*, 2015] firn air trapped at depth could be neglected by commonly applied models of ice shelf firn air content in which firn air thickness is contained within the uppermost densifying layers only, and a density of pure glacial ice is assigned below this layer. Firn air within U4 therefore appears to be an important component of total ice shelf firn air, at inlet sites at least. However, the extent and along-flow geometrical development of U4 is currently unknown as it extends below the base of our down-flow ice shelf boreholes. The fact that our firn air estimates are generally lower than those reported by *Holland et al.* [2011] may indicate that firn air is held within U4 at down-flow sites but was not sampled by our borehole logs. *Craven et al.* [2005] reported the presence of a 205 m thick layer of "white bubbly" continental ice located directly above a marine ice unit at 70 m depth <100 km from the front of Amery Ice Shelf. *Nicholls et al.* [2012] used the water level in two full-thickness boreholes through LCIS to estimate independently the mean density of the shelf, and thus the firn air content, at a northern (-66.87–62.90) and southern (-68.30–63.36) site. This results in firn air contents of 7.2 ± 0.5 m at the northern site and 17.6 ± 0.5 m at the southern site, compared with estimates of 7.8 ± 1.8 m and 15.3 ± 1.8 m after *Holland et al.* [2011] for the same locations.

Our thresholded OPTV logs allow the total proportion of refrozen ice present within each to be approximated. To achieve this, we scale our darkness index percentages to the proportion of the ice column they represent and sum the resulting totals. In all units, except U3 layers, of bright host ice and dark infiltration ice result in algorithm performance that closely matches visual inspection. In these cases we therefore consider our thresholding output to be representative of the percentage of refrozen ice. However, because U3 is composed of alternating layers of ice of different densities, we treat it as a special case and take the unit to have a darkness index of 100%. A further consideration is that as the ice column densifies, the vertical velocity will be preferentially accounted for by the compaction of bubble-rich host ice, not the bubble-poor refrozen ice layers. Consequently, it is expected that refrozen ice will constitute a progressively larger proportion deeper in the ice column given constant levels of melt through time. In the absence of further data, we assign the upper 1.87 m, not sampled by OPTV, a darkness index equal to that of the underlying U1 ice. For 0–90 m depth this analysis results in refrozen ice estimates of 56% at CI-0, 77% at CI-22, 41% at CI-120, 46% at WI-0, and 44% at CI-70.

Inlet sites most affected by föhn warming (CI-0 and CI-22) have notably higher refrozen ice contents than those less affected by intense föhn warming (WI-0, WI-70, and CI-120). The similar refrozen ice contents of the latter three sites suggest that these reflect the effect of ice shelf-wide seasonal warming, melting, and percolation, rather than föhn-driven melting. The relatively low refrozen content at WI-0 may contrast with the conceptual framework of föhn-driven and seasonal melting combining to overprint on the ice column of LCIS. However, we note that the refrozen ice content at WI-0 is inclusive of U4 which has a relative paucity of refrozen ice layers (27.5%; Table 3). The refreezing of meltwater effectively traps firn air at depth, and this effect should be integrated into firn densification models used in correcting altimetric data which otherwise risk underestimating the amount of firn air within the ice column. However, if lateral discontinuities in these melt layers can be exploited then this pore space becomes available to be filled by percolating meltwater.

6. Conclusions

In this study a suite of five optical televiewer (OPTV) logs from the north-central sector of Larsen C Ice Shelf, Antarctica, have been described and analyzed. The ice shelf density structure has been reconstructed based on OPTV image luminosity and the refrozen melt portion based on application of a quantitative thresholding technique. The thresholding performs well when the ice column is composed of densifying, reflective host ice which has been overprinted by layers of refrozen melt, but less well where ice is relatively homogenous as a result of compression or the refreezing of melt ponds. Refrozen ice and remnant refrozen ice makes up >40% of the top 90 m of LCIS and thus is a major contributor to the ice shelf mass redistribution. At inland sites, close to the location of maximum föhn-warming, refrozen ice comprises up to 75% of the top 90 m of the ice column. These observations are brought together to devise a four-part scheme defining distinct ice units. We define U1 as densifying ice shelf accumulation hosting frequent infiltration ice layers; U2 as dense ice also containing frequent infiltration ice layers, distinct from the overlying U1 ice due to a step-change in density; U3 as ice formed by the refreezing of intense föhn-driven surface melt; and U4 as relatively low density (for its depth) continental ice formed upstream of the föhn warming region and advected onto the ice shelf. Where a firn air correction is guided by a firn densification model it neglects the effect of U4 lower density, buried ice from continental sources which may form a significant proportion of the total firn air content at some sites, particularly at locations close to the grounding line.

This research demonstrates the efficacy of hot-water drilling and OPTV borehole logging in acquiring high-resolution structural and melt information from ice shelves. OPTV logging has successfully imaged bubble structures formed during meltwater refreezing, generations of layers that cut across one another formed during ice deformation and fracture close to the grounding line, and refrozen ice layers preserved at depths of up to 90 m. The scheme outlined here could be extended in the future to include other ice shelf ice types such as dry, cold deposited snow devoid of internal melt layers (which we might have termed "U0" had it been present at any of our borehole sites on LCIS), marine ice, or rift ice.

Results of this study indicate that föhn winds and seasonal melting are a major influence on the physical structure of LCIS, which may have implications for ice shelf evolution, modeling, and stability. The ice shelf stratigraphy and structure presented here record changes in ice shelf conditions over time and present an opportunity to inform process models of past surface mass balance and flow. Recent observations and modeling indicate that katabatic winds may also warm inland portions of some other Antarctic ice shelves [Lenaerts et al., 2016]. Future work must therefore elucidate the evolution of other ice shelves and explore structural commonalities as ice shelves across Antarctica experience climate warming. The structural units defined in this study are a source of heterogeneity within the LCIS, in addition to basal and surface crevasses, bands of suture ice, and rifts. This research raises questions about how material heterogeneities influence ice flow and fracture, where ice density is a key parameter, and how these are incorporated into predictive models of ice shelf stability.

References

Banwell, A. F., D. R. MacAyeal, and O. V. Sergienko (2013), Breakup of the Larsen B ice shelf triggered by chain reaction drainage of supraglacial lakes, *Geophys. Res. Lett.*, 40, 5872–5876, doi:10.1002/2013GL057694.

Cape, M. R., M. Vernet, P. Skvarca, S. Marinsek, T. Scambos, and E. Domack (2015), Foehn winds link climate-driven warming to ice shelf evolution in Antarctica, *J. Geophys. Res. Atmos.*, 120, 11,037–11,057, doi:10.1002/2015JD023465.

Chuter, S. J., and J. L. Bamber (2015), Antarctic ice shelf thickness from CryoSat-2 radar altimetry, *Geophys. Res. Lett.*, 42, 10,721–10,729, doi:10.1002/2015GL066515.

Cook, A. J., and D. G. Vaughan (2010), Overview of areal changes of the ice shelves on the Antarctic Peninsula over the past 50 years, *Cryosphere*, 4, 77–98, doi:10.5194/tc-4-77-2010.

Craven, M., F. Carsey, A. Behar, J. Matthews, R. Brand, A. Elcheikh, S. Hall, and A. Treverrow (2005), Borehole imagery of meteoric and marine ice layers in the Amery Ice Shelf, East Antarctica, *J. Glaciol.*, 51(172), 75–84, doi:10.3189/172756505781829511.

De Rydt, J., G. H. Gudmundsson, H. Rott, and J. L. Bamber (2015), Modeling the instantaneous response of glaciers after the collapse of the Larsen B Ice Shelf, *Geophys. Res. Lett.*, 42, 5355–5363, doi:10.1002/2015GL064355.

Dierckx, M., and J.-L. Tison (2013), Marine ice deformation experiments: an empirical validation of creep parameters, *Geophys. Res. Lett.*, 40, 134–138, doi:10.1029/2012GL054197.

Drews, R., J. Brown, K. Matsuoka, E. Witrant, M. Philippe, B. Hubbard, and F. Pattyn (2016), Constraining variable density of ice shelves using wide-angle radar measurements, *Cryosphere*, 10, 811–823, doi:10.5194/tc-10-811-2016.

Elvidge, A. D., I. A. Renfrew, J. C. King, A. Orr, T. A. Lachlan-Cope, M. Weeks, and S. L. Gray (2015), Foehn jets over the Larsen C Ice Shelf, Antarctica, *Q. J. R. Meteorol. Soc.*, 141, 698–713, doi:10.1002/qj.2382.

Glasser, N. F., B. Kulessa, A. Luckman, D. Jansen, E. C. King, P. R. Sammonds, T. A. Scambos, and K. C. Jezek (2009), Surface structure and stability of the Larsen C Ice Shelf, Antarctic Peninsula, *J. Glaciol.*, 55(191), 400–410, doi:10.3189/002214309788816597.

Glasser, N. F., T. Holt, E. Fleming, and C. Stevenson (2014), Ice shelf history determined from deformation styles in surface debris, *Antarct. Sci.*, *26*, 661–673, doi:10.1017/S0954102014000376.

Holland, P. R., H. F. J. Corr, H. D. Pritchard, D. G. Vaughan, R. J. Arthern, A. Jenkins, and M. Tedesco (2011), The air content of Larsen Ice Shelf, *Geophys. Res. Lett.*, *38*, L10503, doi:10.1029/2011GL047245.

Holland, P. R., A. Brisbourne, H. F. J. Corr, D. McGrath, K. Purdon, J. Paden, H. A. Fricker, F. S. Paolo, and A. H. Fleming (2015), Oceanic and atmospheric forcing of Larsen C Ice-Shelf thinning, *Cryosphere*, *9*, 1005–1024, doi:10.5194/tc-9-1005-2015.

Hubbard, B. (1991), Freezing-rate effects on the physical characteristics of basal ice formed by net adfreezing, *J. Glaciol.*, *37*(127), 339–347, doi:10.3198/1991JoG37-127-339-347.

Hubbard, B., and T. Malone (2013), Optical-televiewer-based logging of the uppermost 630 m of the NEEM deep ice borehole, Greenland, *Ann. Glaciol.*, *54*(64), 83–89, doi:10.3189/2013AoG64A201.

Hubbard, B., et al. (2016), Massive subsurface ice formed by refreezing of ice-shelf melt ponds, *Nat. Commun.*, *7*, 11897, doi:10.1038/ncomms11897.

Hubbard, B., S. Roberson, D. Samyn, and D. Merton-Lyn (2008), Digital optical televiewing of ice boreholes, *J. Glaciol.*, *54*(188), 823–830, doi:10.3189/002214308787779988.

Hubbard, B., J.-L. Tison, F. Pattyn, M. Dierckx, T. Boereboom, and D. Samyn (2012), Optical-televiewer-based identification and characterization of material facies associated with an Antarctic ice-shelf rift, *Ann. Glaciol.*, *53*(60), 137–146, doi:10.3189/2012AoG60A045.

Hubbard, B., J.-L. Tison, M. Philippe, B. Heene, F. Pattyn, T. Malone, and J. Freitag (2013), Ice shelf density reconstructed from optical televiewer borehole logging, *Geophys. Res. Lett.*, *40*, 5882–5887, doi:10.1002/2013GL058023.

Hudleston, P. J. (2015), Structures and fabrics in glacial ice: A review, *J. Struct. Geol.*, *81*, 1–27, doi:10.1016/j.jsg.2015.09.003.

Jansen, D., A. Luckman, A. Cook, S. Bevan, B. Kulessa, B. Hubbard, and P. Holland (2015), Brief communication: Newly developing rift in Larsen C Ice Shelf presents significant risk to stability, *Cryosphere*, *9*, 1223–1227, doi:10.5194/tc-9-1223-2015.

Kinnard, C., R. M. Koerner, C. M. Zdanowicz, D. A. Fisher, J. Zheng, M. J. Sharp, L. Nicholson, and B. Lauriol (2008), Stratigraphic analysis of an ice core from the Prince of Wales Icefield, Ellesmere Island, Arctic Canada, using digital image analysis: High-resolution density, past summer warmth reconstruction, and melt effect on ice core solid conductivity, *J. Geophys. Res.*, *113*, D24120, doi:10.1029/2008JD011083.

Kittler, J., and J. Illingsworth (1986), Minimum error thresholding, *Pattern Recognit.*, *19*(1), 41–47, doi:10.1016/0031-3203(86)90030-0.

Kuipers Munneke, P., S. R. M. Ligtenberg, M. R. van den Broeke, and D. G. Vaughan (2014), Firn air depletion as a precursor of Antarctic ice-shelf collapse, *J. Glaciol.*, 60, (220), 205–214, doi:10.3189/2014JoG13J183.

Kulessa, B., D. Jansen, A. Luckman, E. C. King, and P. R. Sammonds (2014), Marine ice regulates the future stability of a large Antarctic ice shelf, *Nat. Commun.*, *5*, 3707, doi:10.1038/ncomms4707.

Lenaerts, J. T. M., et al. (2016), Meltwater produced by wind-albedo interaction stored in an East Antarctic ice shelf, *Nat. Clim. Change*, *7*, 58–62, doi:10.1038/nclimate3180.

Luckman, A., A. Elvidge, D. Jansen, B. Kulessa, P. Kuipers Munneke, J. King, and N. E. Barrand (2014), Surface melt and ponding on Larsen C Ice Shelf and the impact of föhn winds, *Antarct. Sci.*, *26*, 625–635, doi:10.1017/S0954102014000339.

Machguth, H., M. MacFerrin, D. van As, J. E. Box, C. Charalampidis, W. Colgan, R. S. Fausto, H. A. J. Meijer, E. Mosley-Thompson, and R. S. W. van de Wal (2016), Greenland meltwater storage in firn limited by near-surface ice formation, *Nat. Clim. Change*, *6*, 390–393, doi:10.1038/nclimate2899.

Malone, T. S., B. Hubbard, D. Merton-Lyn, P. Worthington, and R. Zwiggelaar (2013), Borehole and Ice Feature Annotation Tool (BIFAT): A program for the automatic and manual annotation of glacier borehole images, *Comput. Geosci.*, *51*, 381–389, doi:10.1016/j.cageo.2012.09.002.

McGrath, D., K. Steffen, H. Rajaram, T. Scambos, W. Abdalati, and E. Rignot (2012), Basal crevasses on the Larsen C Ice Shelf, Antarctica: Implications for meltwater ponding and hydrofracture, *Geophys. Res. Lett.*, *39*, L16504, doi:10.1029/2012GL052413.

McGrath, D., K. Steffen, P. R. Holland, T. Scambos, H. Rajaram, W. Abdalati, and E. Rignot (2014), The structure and effect of suture zones in the Larsen C Ice Shelf, Antarctica, *J. Geophys. Res. Earth*, *119*, 588–602, doi:10.1002/2013JF002935.

Morris, E. M. and D. G. Vaughan (2003), Spatial and temporal variation of surface temperature on the Antarctic Peninsula and the limit of viability of ice shelves, in *Antarctic Peninsula Climate Variability: Historical and Paleoenvironmental Perspectives*, edited by E. Domack, et al., pp. 61–68, AGU, Washington, D. C., doi:10.1029/AR079p0061.

Nicholls, K. W., K. Makinson, and E. J. Venables (2012), Ocean circulation beneath Larsen C Ice Shelf, Antarctica from in situ observations, *Geophys. Res. Lett.*, *39*, L19608, doi:10.1029/2012GL053187.

O'Neill, A. D. J., and D. M. Gray (1973), Solar radiation penetration through snow, in *The Role of Snow and ice in Hydrology: Proceedings of the Bang Symposium*, vol. 1, pp. 227–249, UNESCO-WMO-IAHS, Geneva-Budapest-Paris.

Otsu, N. (1979), A threshold selection method from gray-level histograms, *IEEE Trans. Syst. Man Cybern.*, *9*(1), 62–66, doi:10.1109/TSMC.1979.4310076.

Paolo, F. S., H. A. Fricker, and L. Padman (2015), Volume loss of Antarctic ice shelves is accelerating, *Science*, doi:10.1126/science.aaa0940.

Philippe, M., et al. (2016), Ice core evidence for a 20th century increase in surface mass balance in coastal Dronning Maud Land, East Antarctica, *Cryosphere*, *10*(5), 2501–2516, doi:10.5194/tc-10-2501-2016.

Pritchard, H. D., S. R. M. Ligtenberg, H. A. Fricker, D. G. Vaughan, M. R. van den Broeke, and L. Padman (2012), Antarctic ice-sheet loss driven by basal melting of ice shelves, *Nature*, *484*, 502–505, doi:10.1038/nature10968.

Proksch, M., N. Rutter, C. Fierz, and M. Schneebeli (2016), Intercomparison of snow density measurements: Bias, precision, and vertical resolution, *Cryosphere*, *10*, 371–384, doi:10.5194/tc-10-371-2016.

Ridler, T., and S. Calvard (1978), Picture thresholding using an iterative selection method, *IEEE Trans. Syst. Man Cybern.*, *8*(8), 630–632, doi:10.1109/TSMC.1978.4310039.

Scambos, T., H. A. Fricker, C.-C. Liu, J. Bohlander, J. Fastook, A. Sargent, R. Massom, and A.-M. Wu (2009), Ice shelf disintegration by plate bending and hydro-fracture: Satellite observations and model results of the 2008 Wilkins ice shelf break-ups, *Earth Planet. Sci. Lett.*, *280*(1–4), 51–60, doi:10.1016/j.epsl.2008.12.027.

Scambos, T. A., J. A. Bohlander, C. A. Shuman, and P. Skvarca (2004), Glacier acceleration and thinning after ice shelf collapse in the Larsen B embayment, *Geophys. Res. Lett.*, *31*, L18402, doi:10.1029/2004GL020670.

Scambos, T., C. Hulbe, and M. Fahnestock (2003), Climate-induced ice shelf disintegration in the Antarctic Peninsula, in *Antarctic Peninsula Climate Variability: Historical and Paleoenvironmental Perspectives*, edited by E. Domack, et al., pp. 72–92, AGU, Washington, D. C., doi:10.1029/AR079p0079.

Turner, J., H. Lu, K. White, J. C. King, T. Phillips, J. S. Hosking, T. J. Bracegirdle, G. J. Marshall, R. Mulvany, and P. Deb (2016), Absence of 21st century warming on Antarctic Peninsula consistent with natural variability, *Nature*, *535*, 411–441, doi:10.1038/nature18645.

van Wessem, J. M., et al. (2016), The modelled surface mass balance of the Antarctic Peninsula at 5.5 km horizontal resolution, *Cryosphere*, *10*, 271–285, doi:10.5194/tc-10-271-2016.